

See discussions, stats, and author profiles for this publication at: <https://www.researchgate.net/publication/264635698>

# Full-Field Dynamic Characterization of Superhydrophobic Condensation on Biотemplated Nanostructured Surfaces

ARTICLE in LANGMUIR · MAY 2014

Impact Factor: 4.46 · DOI: 10.1021/la501063j · Source: PubMed

---

CITATIONS

9

READS

28

## 5 AUTHORS, INCLUDING:



E. Ölçeroğlu

Drexel University

9 PUBLICATIONS 28 CITATIONS

[SEE PROFILE](#)



Chia-Yun Hsieh

Drexel University

8 PUBLICATIONS 209 CITATIONS

[SEE PROFILE](#)



Md Mahamudur Rahman

Drexel University

9 PUBLICATIONS 26 CITATIONS

[SEE PROFILE](#)



Kenneth Lau

Drexel University

72 PUBLICATIONS 2,348 CITATIONS

[SEE PROFILE](#)

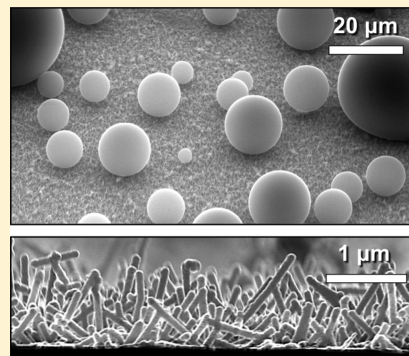
## Full-Field Dynamic Characterization of Superhydrophobic Condensation on Biotemplated Nanostructured Surfaces

Emre Ölçeroğlu,<sup>†</sup> Chia-Yun Hsieh,<sup>‡</sup> Md Mahamudur Rahman,<sup>†</sup> Kenneth K. S. Lau,<sup>‡</sup> and Matthew McCarthy\*,<sup>†</sup>

<sup>†</sup>Department of Mechanical Engineering and Mechanics, and <sup>‡</sup>Department of Chemical and Biological Engineering, Drexel University, 3141 Chestnut Street, Philadelphia, Pennsylvania 19104, United States

### Supporting Information

**ABSTRACT:** While superhydrophobic nanostructured surfaces have been shown to promote condensation heat transfer, the successful implementation of these coatings relies on the development of scalable manufacturing strategies as well as continued research into the fundamental physical mechanisms of enhancement. This work demonstrates the fabrication and characterization of superhydrophobic coatings using a simple scalable nanofabrication technique based on self-assembly of the *Tobacco mosaic virus* (TMV) combined with initiated chemical vapor deposition. TMV biotemplating is compatible with a wide range of surface materials and applicable over large areas and complex geometries without the use of any power or heat. The virus-structured coatings fabricated here are macroscopically superhydrophobic (contact angle >170°) and have been characterized using environmental electron scanning microscopy showing sustained and robust coalescence-induced ejection of condensate droplets. Additionally, full-field dynamic characterization of these surfaces during condensation in the presence of noncondensable gases is reported. This technique uses optical microscopy combined with image processing algorithms to track the wetting and growth dynamics of 100s to 1000s of microscale condensate droplets simultaneously. Using this approach, over 3 million independent measurements of droplet size have been used to characterize global heat transfer performance as a function of nucleation site density, coalescence length, and the apparent wetted surface area during dynamic loading. Additionally, the history and behavior of individual nucleation sites, including coalescence events, has been characterized. This work elucidates the nature of superhydrophobic condensation and its enhancement, including the role of nucleation site density during transient operation.



## INTRODUCTION

Condensation heat transfer is found in a wide range of real-world applications and industries including power generation, thermal management, chemical processing, water purification, and HVAC. Additionally, condensation plays a critical role in the performance of new applications and materials such as biomimetic surfaces for self-cleaning, antifouling, and water harvesting. It has been shown that coatings composed of high-surface-area micro/nanostructures can be used to substantially enhance condensation,<sup>1,2</sup> as well as a variety of other phase-change heat transfer processes including boiling, evaporation, and freezing.<sup>3–6</sup> Superhydrophobic nanostructured coatings drastically reduce surface wettability and demonstrate extreme water repellency, where near-spherical droplets rest on top of the surface structures with contact angles approaching 180°. They have been fabricated using a wide array of techniques including direct etching,<sup>5,7,8</sup> oxidation and growth of nanostructures,<sup>1,9,10</sup> molding,<sup>11</sup> biotemplating,<sup>12</sup> and electrodeposition.<sup>13</sup> Such surfaces have received attention for applications in self-cleaning,<sup>12</sup> reducing heat transfer during freezing to create anti-icing coatings,<sup>5,14</sup> as well as increasing heat transfer efficiency during condensation.<sup>1,15</sup>

Dropwise condensation onto hydrophobic surfaces (where condensate forms into millimeter-scale droplets) is much more efficient than filmwise condensation (where condensate forms into liquid films), due to the shedding of condensate by gravity.<sup>16,17</sup> “Jumping-mode” superhydrophobic condensation has been demonstrated more recently, where microscale droplets undergo coalescence-induced ejection.<sup>2</sup> When one or more near-spherical droplets condense onto a superhydrophobic surface and coalesce with each other, the excess energy due to decreased surface area is converted into kinetic energy, leading to droplet ejection. This mechanism delays the formation of an insulating liquid layer and shows great promise for increasing efficiencies in condensation heat transfer systems. Boreyko and Chen demonstrated self-ejecting microscale droplets using two-tiered hierarchical structures composed of carbon nanotubes and etched silicon pillars.<sup>2</sup> This observed phenomenon has led to extensive research into in situ imaging of nanoscale condensate droplets using environmental electron scanning microscopy (ESEM),<sup>18–21</sup> as well as various

Received: March 20, 2014

Revised: May 28, 2014

Published: May 31, 2014

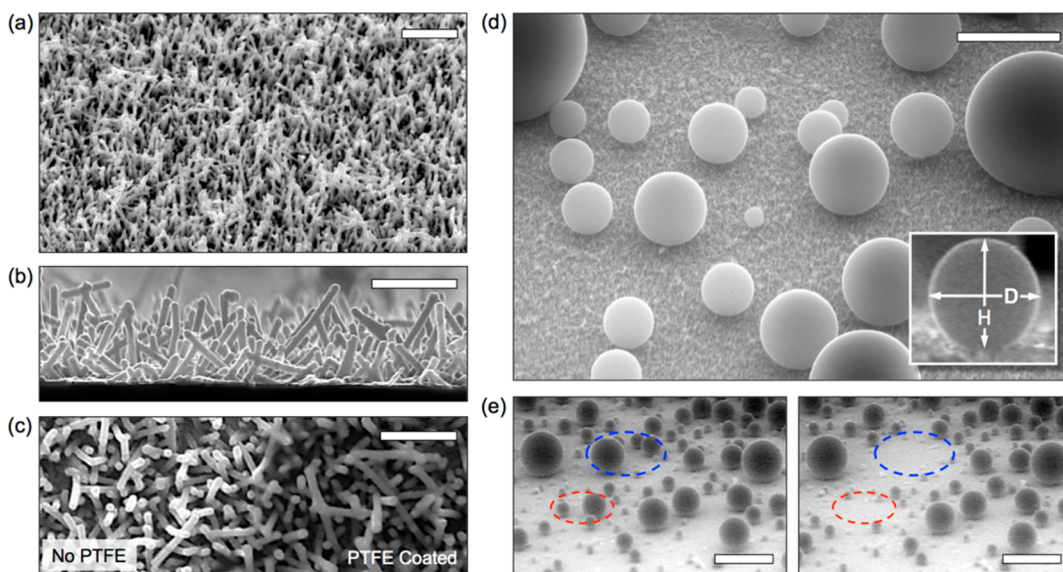


**Figure 1.** Biotemplated superhydrophobic coatings. SEM images showing (a) oblique and (b) cross-sectional side views of nickel nanostructures fabricated using the self-assembly and metallization of the *Tobacco mosaic virus*. Scale bars are (a) 2  $\mu\text{m}$  and (b) 1  $\mu\text{m}$ . (c) SEM image of 10 nm thick PTFE coating using iCVD, showing TMV nanostructures with (right) and without (left) PTFE. Scale bar is 1  $\mu\text{m}$ . (d) Environmental SEM (ESEM) imaging showing superhydrophobic behaviors for microscale condensate droplets. Scale bar is 20  $\mu\text{m}$ , and inset shows high-inclination measurement of droplet diameter and height. (e) ESEM video capture (frames are 10 s apart) showing coalescence-induced ejection of droplets. Scale bars are 100  $\mu\text{m}$ . see Supporting Information for ESEM imaging details and videos.

experimental and theoretical investigations into coalescence-induced jumping of microscale droplets<sup>22,23</sup> and devices based on the principle.<sup>24,25</sup> Taking direct measurements of jumping-mode condensation heat transfer on copper oxide nanostructures, increases in heat transfer coefficients of 30% as compared to smooth hydrophobic surfaces were reported by Miljkovic et al.<sup>1</sup> Additionally, they showed that, once flooded, the nanostructured surfaces performed worse than flat hydrophobic surfaces due to excessive pinning of droplets. This demonstrates the importance of nucleation, wetting, and droplet dynamics on heat transfer during jumping-mode superhydrophobic condensation. Accordingly, Miljkovic et al. and Enright et al. have undertaken a detailed investigation of morphology and wetting dynamics during jumping-mode condensation, creating a modeling framework to predict whether droplets that have nucleated within regularly ordered micro- and nanopillars will emerge into suspended (or partially wetted) mobile droplets or stay pinned to the surface, leading eventually to flooding of the nanostructures.<sup>13,15,26,27</sup>

## FABRICATION

The implementation of superhydrophobic condensation into real-world applications requires the development of scalable fabrication techniques capable of coating large areas, complex geometries, and various surface materials. In this work, superhydrophobic nanostructured surfaces were created using a solution-based biotemplating technique based on self-assembly and metallization of the *Tobacco mosaic virus* (TMV), combined with hydrophobic functionalization using initiated chemical vapor deposition (iCVD) of thin polymer coatings. These manufacturing methods are room temperature processes and scalable to large areas, complex geometries, and nearly any surface material, making them attractive for implementation in real-world heat transfer systems. TMV biotemplating has been previously demonstrated on silicon, aluminum, stainless steel, copper, and various polymeric

surfaces, including conformal coatings onto complex 3D microstructures.<sup>6,12,28–30</sup> iCVD has been used to deposit uniform nanoscale films conformally around individual nanostructures, where the composition is essentially identical to bulk PTFE, as shown using FTIR spectroscopy.<sup>10,31</sup> Additionally, iCVD has been demonstrated as a scalable fabrication method with the potential for widespread adoption, similar to the importance of CVD processing in enabling the semiconductor and integrated circuit industry.<sup>32,33</sup>

**Virus-Templated Nanostructured Coatings.** The TMV is used as a biological template to fabricate conformal coatings of high-aspect-ratio nanostructures.<sup>34</sup> The TMV is a well-researched cylindrical biomacromolecule (300 nm length, 18 nm diameter) composed of over 2000 coat proteins wrapped in a helical arrangement around a single strand of plus sense RNA.<sup>35</sup> It is benign to humans and stable at temperatures of up to 60 °C and a pH of 3.5–9. It can be safely, sustainably, and cheaply replicated in large quantities through the infection of the tobacco plant. The repeating arrangements of charged amino acids along the surface of the TMV virion can function in the nucleation of inorganic precursors, facilitating the metallization or mineralization of the virus. Nanoparticles and nanowires have been synthesized in solution using the wild-type virus coated with various materials both on and within the virus structure.<sup>36–38</sup> Additionally, cysteine binding sites have been introduced using genetic modifications to facilitate self-assembly and metallization in a near-vertical arrangement onto various surfaces.<sup>28,39</sup> Using this modification, surface-bound TMV has been demonstrated for enhancing microbatteries,<sup>29,40–42</sup> light-harvesting systems,<sup>43</sup> and surface wettability.<sup>6,12</sup>

This genetic modification (TMV1cys) is used here to produce nanostructured coatings on gold-coated silicon chips using a solution-based room temperature process. First, the chips are submerged in a 0.1 g/L virus solution for 24 h, where the TMV naturally self-assembles onto the surface. This is

followed by immersion in a palladium catalyst bath for 2–3 h where palladium nanoclusters form on the TMV surface. Finally, the samples are placed in an electroless nickel plating solution for 2–5 min, where a thin shell of nickel is electrolessly deposited onto the palladium catalyst. The virus acts only as a temporary scaffold for the deposition of nickel and has no effect in maintaining the nanostructure afterward. Figure 1a,b shows SEM images of the resulting nanostructured coatings at two magnifications and orientations, where the resulting high-surface-area nickel nanocoatings are  $\sim 1 \mu\text{m}$  tall with individual nanostructures  $\sim 100 \text{ nm}$  in diameter. This process has been demonstrated in previous publications<sup>30,34</sup> and described in more detail in the Supporting Information section 2.1.

**Initiated Chemical Vapor Deposition.** To create superhydrophobic surfaces, the virus-structured nickel nanocoatings shown in Figure 1a,b were functionalized with a thin coating of polytetrafluoroethylene (PTFE) using initiated chemical vapor deposition (iCVD). iCVD is a proven one-step technique for achieving conformal, uniform, and ultrathin PTFE films.<sup>10,31,44,45</sup> It has distinct advantages over other methods such as hot-filament chemical vapor deposition (HFCVD),<sup>46</sup> plasma-enhanced CVD,<sup>47,48</sup> laser deposition,<sup>49</sup> and electrospraying,<sup>50</sup> which typically involve more than one step and result in thicker films or nonstoichiometric “PTFE-like” films. Additionally, iCVD of grafted polymer films has been successfully demonstrated on flat surfaces for the realization of stable dropwise condensation.<sup>51</sup> The details of the iCVD process have been described previously.<sup>52–55</sup> Briefly, iCVD PTFE synthesis involves (1) the introduction of hexafluoropropylene oxide vapor as monomer and nonafluorobutane-sulfonyl fluoride as initiator into the iCVD reactor chamber; (2) thermal activation of the initiator vapor using an array of resistively heated filament wires at  $300^\circ\text{C}$ ; (3) adsorption of both activated initiator and monomer onto the sample surface which is cooled using a recirculating bath at  $20^\circ\text{C}$ ; and (4) polymerization–codeposition on the cooled surface by addition of monomer units to the activated initiator sites. Complete details of the iCVD process and reactor chamber can be found in the Supporting Information section 2.2.

In this work, the thickness of the PTFE film was monitored *in situ* using an interferometry system that tracks the deposition rate in real-time as the deposition occurs. This system is equipped with a 633 nm HeNe laser (JDS Uniphase) and it reaches into the reaction zone through a glass window on top of the chamber.<sup>56</sup> Figure 1c shows an SEM image of the resulting 10 nm thick PTFE coating deposited conformally onto the complex TMV nanostructure geometry, as compared to an area not coated with PTFE. This was achieved using a standard photoresist lift-off process. The resulting superhydrophobic nanostructured surfaces have equilibrium contact angles of  $\sim 170^\circ$ , as well as roll-off tilt angles and contact angle hysteresis values well below  $2^\circ$ , consistent with previous findings.<sup>12</sup>

## ■ WETTING AND DROPLET MORPHOLOGY

While macroscale measurements show that the surfaces are nearly perfectly superhydrophobic, environmental scanning electron microscopy was used to characterize the microscale wetting dynamics and droplet morphologies during condensation. An FEI XL30 ESEM was operated in wet-mode and coupled with a thermoelectric stage to subcool the samples. The chamber was filled with water vapor at  $4.4 \pm 0.5 \text{ Torr}$ , and the cold stage was initially brought down to the saturation

temperature. Once the sample temperature reaches equilibrium, it was then incrementally subcooled by  $\sim 1^\circ\text{C}$  to initiate condensation, corresponding to a supersaturation of  $S = 1.06$ . Supersaturation is defined as the ratio of vapor pressure to the saturation pressure corresponding to the surface temperature.

Figure 1d shows near-spherical microscale condensate droplets with diameters smaller than  $5 \mu\text{m}$ . A high-inclination viewing angle was used to characterize the large apparent contact angles of the droplets. By measuring the height and diameter, as shown in the inset of Figure 1d, the apparent contact angle can be geometrically determined (Supporting Information section 3.1). Figure 2 shows the measured

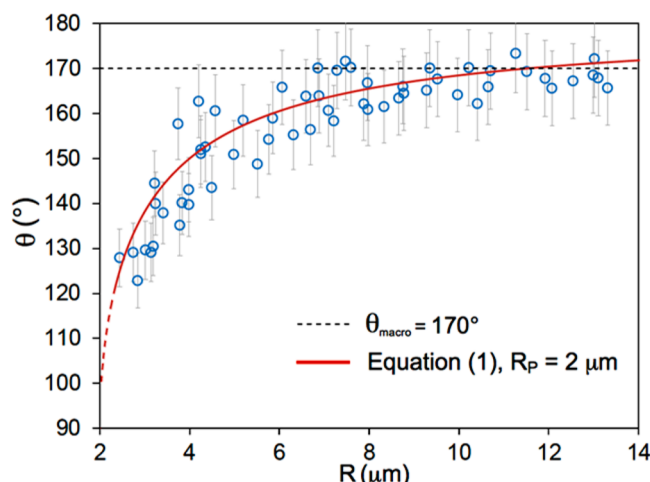


**Figure 2.** Droplet apparent contact angle as a function of radius, measured from ESEM images, plotted against eq 1 and the macroscopically measured apparent contact angle.

apparent contact angle ( $\theta$ ) as a function of radius ( $R$ ) where contact angle decreases with droplet size, plotted against the macroscopically measured value. It can be seen that the contact angles are approximated well (for radius of  $2.5\text{--}11 \mu\text{m}$ ) using a curve fit of the form

$$\theta = \cos^{-1}\left(\frac{R_p}{R}\right) + \frac{\pi}{2} \quad (1)$$

where  $R_p$  is representative of the pinned diameter at the droplet base. This measurement and curve fitting technique was demonstrated by Enright et al. for micro/nanostructured surfaces.<sup>13</sup>

Figure 1e shows coalescence-induced ejection where two or more droplets coalesce, and the excess surface energy is converted to kinetic energy, resulting in the characteristic jumping phenomena. The surfaces demonstrated continuous and stable coalescence-induced ejection for supersaturations of  $S = 1.06\text{--}1.12$ , with no breakdown or flooding. ESEM movies of jumping-mode superhydrophobic condensation on the iCVD-functionalized biotemplated nanostructured surfaces can be found in the corresponding Supporting Information.

## ■ EXPERIMENTAL CHARACTERIZATION

**Optical Microscopy of Superhydrophobic Condensation.** While ESEM is useful for understanding the morphology and wetting dynamics of individual droplets, it has several inherent limitations. It cannot characterize the full-field dynamics of droplet nucleation, growth, and ejection during

superhydrophobic condensation due to slow imaging times and is limited to a narrow range of operating pressures and temperatures. Additionally, beam heating effects complicate the measurement of temperatures and heat fluxes and can damage the surface leading to artificially increased nucleation sites densities.<sup>13,21</sup> While recent work has focused on mitigating these effects and has demonstrated impressive results using ESEM,<sup>15,19,20</sup> the current work focuses on optical microscopy techniques combined with image processing for the full-field dynamic characterization of superhydrophobic condensation. A custom-built test apparatus (Figure S3) was used to control the environmental conditions within a chamber directly below the objective of an upright optical microscope (Nikon Eclipse LV150) fitted with a high-speed camera (Phantom V210). The surface temperature of the samples was controlled using a cold plate and a circulating bath, while the saturation conditions within the chamber were controlled using nitrogen sparged through water and measured using a high-sensitivity humidity probe (Rotronic HC2-S). Complete details of the experimental setup are explained in the Supporting Information section 3.2. Using this setup, jumping-mode superhydrophobic condensation was characterized in the presence of noncondensable gases (NCGs). This setup allows for the investigation of the effects of loading and ramp rate on droplet density, size distribution, wetting states, and overall heat transfer performance.

The four distinct experimental conditions studied in this work are shown in Table 1. The steady-state saturation

**Table 1. Experimental Test Conditions for Superhydrophobic Condensation in the Presence of Noncondensable Gases**

test name	ramp speed	$T_s$ (°C)	$T^\infty$ (°C)	RH (%)	$\Delta T_{\text{sat}}^\infty$ (°C)	$\Delta T_{\text{sat}}^i$ (°C)
S_2.5	slow, $\tau = 75$ s	13.4	19.7	79.2	2.6	0.011
F_2.5	fast, $\tau = 25$ s	13.5	19.2	82.1	2.5	0.011
S_6.5	slow, $\tau = 75$ s	7.3	20.2	67.0	6.6	0.017
F_6.5	fast, $\tau = 25$ s	7.6	19.0	72.8	6.4	0.017

temperature difference between the sample surface and the vapor in the chamber ( $\Delta T_{\text{sat}}^\infty$ ) was set to be either 2.5 or 6.5 °C, and the system was allowed to reach steady state at either a “fast” or “slow” rate. Figure S4 (in the Supporting Information) shows the dynamic thermal loading of the samples for all four conditions, where the fast ramp rates reached ~90% of the equilibrium value within 25 s, while the slow ramp rates reached ~90% equilibrium within 75 s. Table 1 lists the ramp speed ( $\tau$ ) and the steady-state values for surface temperature ( $T_s$ ), chamber temperature ( $T^\infty$ ), relative humidity (RH), and saturation temperature difference ( $\Delta T_{\text{sat}}^\infty$ ) for the four cases investigated here. Complete details of the testing procedures can be found in the Supporting Information section 3.2.

During testing the, 1 megapixel high-speed camera records images at 3 fps starting before the initial onset of droplet nucleation and continues for roughly 12 min (>700 s). Full-length videos of each of the four tests performed in this work can be found in the Supporting Information. Figure 3a shows a representative set of time-lapse images over the course of one test, where the field of view of the frames is just over 0.5 mm × 0.5 mm. This was chosen to maximize image resolution while also capturing a large number of droplets in each frame. Each of the testing conditions investigated here yielded sustained and complete jumping-mode superhydrophobic condensation,

where the repeatable nucleation, coalescence, and ejection from active nucleation sites can be seen. The surfaces showed negligible variations in performance across the entirety of each 1 cm × 1 cm chip, as well as good consistency between the various chips fabricated. Due to the stability of the iCVD PTFE coatings,<sup>51</sup> the samples fabricated in this work remained superhydrophobic over the course of 2 months with periodic noncontinuous use. They were regularly cleaned, using solvents and air plasma, and tested multiple times with no visible degradation in performance. While the stability and reliability of superhydrophobic surfaces for long-term condensation applications is still being investigated,<sup>57</sup> the surfaces fabricated in this work have been tested continuously for over 24 h showing repeatable and sustained jumping-mode operation (see Supporting Information section 5 and movies). This suggests that degradation from test to test and variations across different samples was not a factor in this work.

After the experiments were completed, the recorded movies were decomposed into image files for each individual frame (>2000 files per movie), which were then fed into a droplet detection algorithm using MATLAB. The location ( $x$ - $y$  coordinates) and radii of each droplet were measured for each frame in the entire movie. This corresponds to 300–1900 droplets per frame and up to 1 million measurements per movie. For the camera resolution and microscope objective used in this work (20 $\times$ ), one pixel was equivalent to ~1  $\mu\text{m}$ . This resulted in a minimum detectable droplet diameter of 2.5  $\mu\text{m}$  (~2–3 pixels) with an estimated measurement uncertainty of  $\pm 0.5 \mu\text{m}$  (half a pixel). Growth from the critical radius of nucleation to the minimal detected radius (1.25  $\mu\text{m}$ ) was observed to occur extremely fast (< 1 s), and calibration tests at higher magnifications (100 $\times$ ) were used to verify that smaller droplets were not present on undetected nucleation sites. Complete details of the droplet detection and tracking algorithm are given in the Supporting Information section 3.3.

Using this process, the history of an individual nucleation site can be characterized, including the coalescence and ejection of groups of droplets. Figure 3b,c shows magnified images of two groups of droplets before and after a coalescence event (0.33 s apart), where the red circles indicate the droplet on the “primary” nucleation site, which coalesces with the neighboring green droplets. Figure 3d,e shows the corresponding radius as a function of time for the primary nucleation sites shown in Figure 3b,c, respectively. The droplets in Figure 3b undergo repeated coalescence-induced ejection, as seen in Figure 3d, where a new droplet nucleates after each ejection event. The droplets in Figure 3c coalesce but do not immediately eject, leaving the larger blue droplet behind. This is shown in Figure 3e, where an abrupt increase in droplet radius is seen. The droplets eventually eject during a later coalescence event, and the process repeats continually. The measurement technique presented in this work allows for the direct quantitative characterization of the history of each active nucleation site, over the entire duration of the experiment and over areas much larger than the characteristic droplet coalescence length (the average distance between sites).

**Droplet Growth Rate.** Using the image processing data from each movie, the growth rate of individual droplets has been characterized. Figure 4 shows droplet radius as a function of time for more than 20 individual droplets extracted from the two videos captured at  $\Delta T_{\text{sat}}^\infty = 6.5$  °C. Droplets are chosen from random locations across the entire duration of both the “fast” and “slow” ramp rates. The corresponding data for the

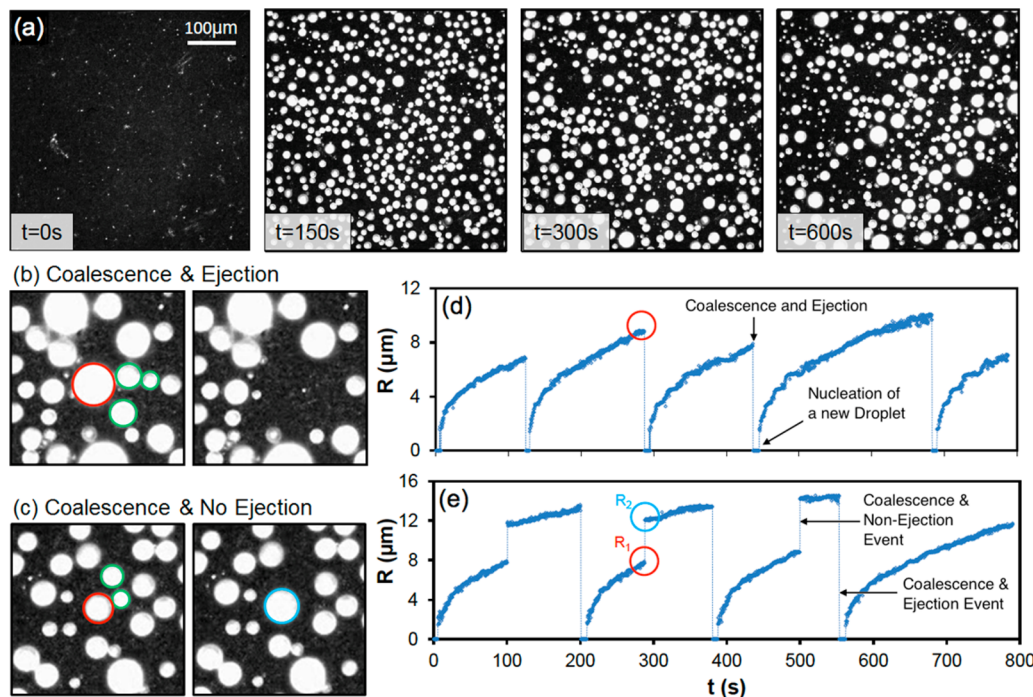


**Figure 3.** Optical microscopy of droplet nucleation, growth, coalescence, and ejection. (a) Time-lapse imaging of superhydrophobic condensation captured using optical microscopy. Showing the ability to characterize (b) coalescence and ejection as well as (c) coalescence and non-ejection of microscale droplets. (d,e) Radius versus time plots for the red nucleation sites shown in (b) and (c), respectively. In (b) and (c), the green droplets coalesce with the primary red droplet, while the resulting coalesced droplet is ejected in (b) and remains on the surface (shown in blue) in (c).

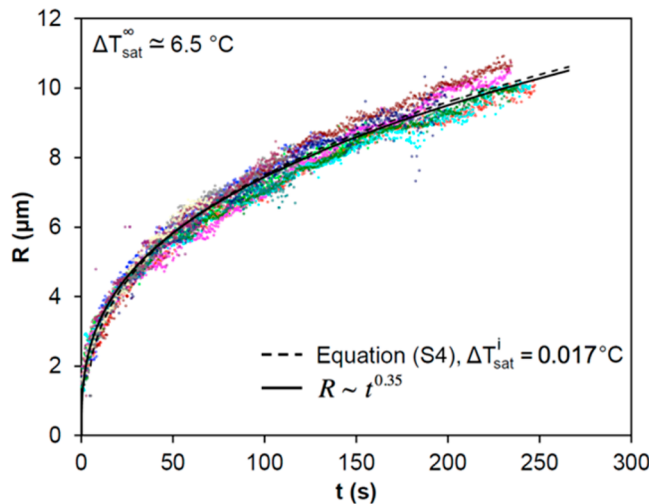


**Figure 4.** Droplet growth rate at  $\Delta T_{\text{sat}}^{\infty} = 6.5 \text{ } ^\circ\text{C}$ , showing radius as a function of time for 20 separate droplets (from both the fast and slow ramp tests), plotted against the thermal circuit model prediction (dashed line) and a power-law fit (solid line).

videos captured at  $\Delta T_{\text{sat}}^{\infty} = 2.5 \text{ } ^\circ\text{C}$  is shown in Figure S7 in the Supporting Information. These droplet growth rates are superimposed onto one another starting at the moment of droplet nucleation continuing until coalescence. These data include droplets with a wide range of sizes and coalescence lengths, as well as droplets that have undergone coalescence and non-ejection events (as shown in Figure 3e), where even after combining with neighboring droplets the growth rates are consistent. The growth rate data in Figure 4 are plotted against a power-law fit (solid line) as well as modeling predictions (dashed line) based on thermal circuit analysis (see Supporting

Information section 4.1 for details). The power-law fit is of the form

$$R = Bt^C \quad (2)$$

where  $B$  and  $C$  are empirically derived constants. As shown in Figure 4 and Figure S7, all of the droplets measured in this work (including all four test conditions) are approximated well using a power coefficient of  $C = 0.35$ . While the proportionality constant  $B$  was independent of ramp rate, but varied with  $\Delta T_{\text{sat}}^{\infty}$  as would be expected. These results are consistent with previous investigations of Beysens<sup>58</sup> and Fritter et al.,<sup>59</sup> where droplet size was found to increase with time raised to the power of  $\sim 1/3$  for the first stage of growth before coalescence. Similarly, Narhe et al. measured condensation growth rates on superhydrophobic surfaces under test conditions comparable to the current work and calculated a coefficient of  $\sim 0.4$ .<sup>60</sup> In other notable works, the initial stage of growth was expected to be  $\sim 1/3$  but was either not measured due to testing limitations<sup>2</sup> or measured in ESEM, leading to increased values attributed to low pressures.<sup>15</sup>

The experimental apparatus allows for precise control of the temperature difference between the superhydrophobic surface and the saturation temperature of the water vapor within the chamber ( $\Delta T_{\text{sat}}^{\infty} = T_{\text{sat}}^{\infty} - T_s$ ). This, however, is not an accurate representation of the saturation conditions near the surface due to the large amount of NCGs in the system. Mass diffusion through the noncondensable nitrogen will reduce the concentration of water vapor near the surface, leading to a dramatic decrease in saturation temperature near the liquid–vapor interface ( $T_{\text{sat}}^i$ ). The interfacial saturation temperature difference ( $\Delta T_{\text{sat}}^i = T_{\text{sat}}^i - T_s$ ) has been determined using closed-form thermal circuit modeling of microscale condensate droplets on superhydrophobic surfaces, as first reported and experimentally validated by Miljkovic et al.<sup>15</sup> This model

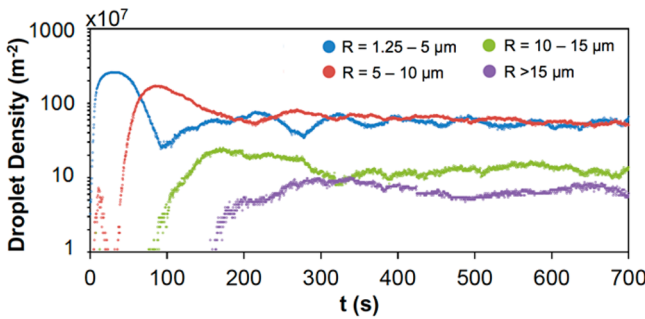


**Figure 5.** Time-varying droplet density and size distribution for  $\Delta T_{\text{sat}}^{\infty} = 6.5 \text{ }^{\circ}\text{C}$  and a slow ramp (test S\_6.5 from Table 1). Experimental uncertainty in droplet density is estimated to be  $\pm 4\%$ .

evaluates the thermal resistance from the saturated vapor (near the interface) through a droplet of known size and apparent contact angle and into a nanostructured surface of known dimensions, material properties, and temperature. By relating the heat transfer rate given by this model to the growth rate of the droplet (and solving numerically), radius as a function of time can be determined. Figure 4 and Figure S7 show good agreement between this model and the experimental results obtained here, predicting interfacial saturation temperature differences ( $\Delta T_{\text{sat}}^i$ ) notably less than the chamber saturation temperature difference ( $\Delta T_{\text{sat}}^{\infty}$ ). These values are consistent to first-order with simplified one-dimensional mass diffusion predictions. As shown, the saturation temperature difference near the liquid–vapor interface was independent of ramp rate, but varied with  $\Delta T_{\text{sat}}^{\infty}$  as would be expected. Complete details of the thermal circuit model can be found in the Supporting Information section 4.1, while Table 1 lists the interfacial saturation temperature differences determined for each test.

**Dynamic Full-Field Characterization.** In addition to capturing the history of individual nucleation sites and droplet growth rates, the combination of optical microscopy and image tracking presented in the work has been used for dynamic full-field characterization of superhydrophobic condensation in the presence of NCGs. Time-varying characteristics of the samples (both surface-averaged and cumulative in nature) can be evaluated using the measured radii for each droplet in each frame of the movies. Figure 5 shows droplet density (the number of droplets per unit area) for several ranges of radius as a function of time, for  $\Delta T_{\text{sat}}^{\infty} = 6.5 \text{ }^{\circ}\text{C}$  with a slow ramp rate. The complete data for droplet size distribution, including dynamic variations and steady-state values for each test, are included in the Supporting Information section 3.4 and Figure S6. Dynamic variations in droplet size distribution can be seen during an initial transient phase, eventually leveling off to steady-state behavior. During steady state, there is approximately the same number of droplets with radii less than  $5 \text{ }\mu\text{m}$ , as those with radii between  $5$  and  $10 \text{ }\mu\text{m}$ . The densities of the larger radii ranges are roughly an order of magnitude less, suggesting a surface-averaged coalescence length close to, but below,  $20 \text{ }\mu\text{m}$ .

Figure 6 shows active nucleation site density ( $N$ ), average droplet radius ( $\bar{R}$ ), and total surface heat flux ( $\dot{Q}''$ ) as a function of time for all four testing conditions, showing the impact of saturation temperature difference as well as ramp rate.  $N$  is calculated by simply adding up the number of droplets in each frame, while  $\bar{R}$  is the arithmetic mean of the detected droplets in each frame. The total heat flux is calculated as

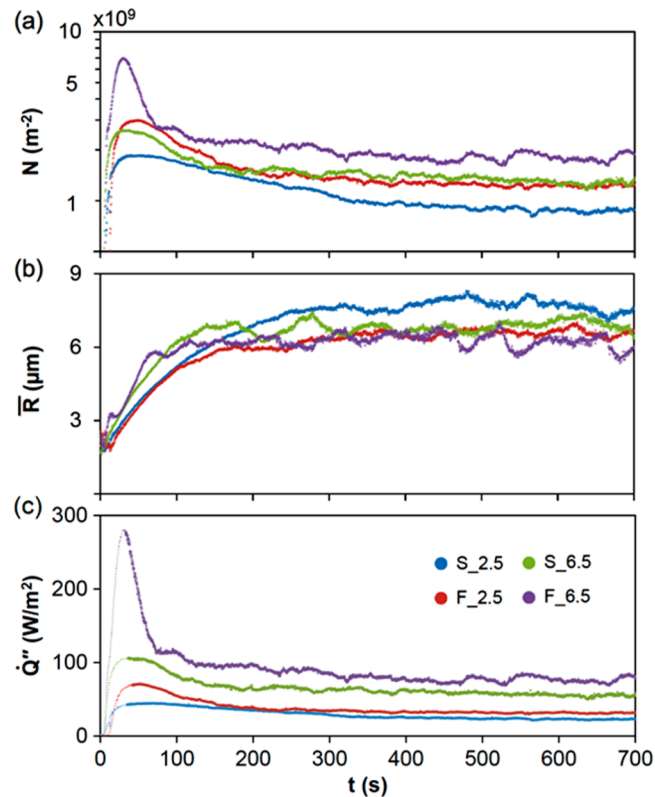


**Figure 6.** Time-varying (a) active nucleation site density,  $N$ , (b) average droplet radius,  $\bar{R}$ , and (c) total surface heat flux,  $\dot{Q}''$ , as a function of time for the four test conditions from Table 1. Experimental uncertainties are estimated to be  $\pm 4$ ,  $\pm 6$ , and  $\pm 17\%$ , respectively. The dotted lines in (c) represent data with an uncertainty  $>30\%$ , due to the large uncertainty in droplet growth rate at small average radii.

$$\dot{Q}'' = \frac{1}{A} \sum_j^N \dot{q}_{\text{drop}} \quad (3)$$

where  $A$  is the area of the field of view ( $525 \text{ }\mu\text{m} \times 525 \text{ }\mu\text{m}$ ). The heat transfer rate through an individual droplet is calculated by evaluating its volumetric growth rate

$$\dot{q}_{\text{drop}} = \dot{m} h_{\text{fg}} = \rho_w h_{\text{fg}} \frac{dV}{dt} \quad (4)$$

where  $\rho_w$  and  $h_{\text{fg}}$  are the liquid density and latent heat of vaporization of water, respectively. By differentiating the volume of a truncated spherical droplet with respect to time, the growth rate ( $dV/dt$ ) can be rewritten, yielding

$$\begin{aligned} \dot{q}_{\text{drop}} = \pi \rho_w h_{\text{fg}} R^2 \frac{dR}{dt} \\ \times \left[ (1 - \cos^2 \theta) \sin \theta \frac{d\theta}{dR} R + (1 - \cos \theta)^2 \right. \\ \left. (2 + \cos \theta) \right] \end{aligned} \quad (5)$$

where  $\theta$  is the apparent contact angle of the droplet. The total surface heat flux at each time step is calculated using eq 3 by adding up the heat transfer rates of each individual droplet on the surface, as given by eq 5. For each droplet, the radius is measured using image processing and the apparent contact angle is given by eq 1, with minimum and maximum bounds of

120 and 170°, respectively, consistent with ESEM and macroscopic measurements. The  $dR/dt$  and  $d\theta/dR$  terms are calculated by differentiating the experimentally validated approximations given by eqs 1 and 2 and evaluating them at the measured droplet radius.

The minimal detected droplet radius was  $R_{\min} \sim 1.25 \mu\text{m}$ , meaning that any heat transferred prior to the droplet reaching this size is not being accounted for. The error being introduced by this can be estimated using both the experimentally measured droplet growth rates, as well as simple examination of existing analytical models for superhydrophobic condensation (Supporting Information section 4.2.1). This error has been shown to vary from ~0.2 to 5% over the range of conditions used in this work, with over 85% of those measurements having errors falling below 2%, suggesting that this effect has a minimal impact on the overall experimental accuracy. This is due to the extremely fast growth rates at these small droplet sizes, resulting in short durations over which the droplets are below the minimum detectable radius. The uncertainty in the measurement of total surface heat flux has been conservatively estimated to be  $\pm 17\%$ , including the propagation of error from other measured quantities ( $\pm 12\%$ ) as well as the error associated with minimum detectable radius ( $\pm 5\%$ ). Complete details the calculation of heat flux as a function of droplet radius as well as its error can be found in the Supporting Information Section 4.2.

To correlate overall heat transfer performance with wetting and droplet dynamics, three relevant area ratios are calculated as

$$\frac{A_p}{A} = \frac{1}{A} \sum_j^N A_{p,drop} \quad (6)$$

$$\frac{A_i}{A} = \frac{1}{A} \sum_j^N A_{i,drop} \quad (7)$$

$$\frac{A_w}{A} = \frac{1}{A} \sum_j^N A_{w,drop} \quad (8)$$

and plotted in Figure 7 as a function of time, where

$$A_{p,drop} = \pi R^2 \quad (9)$$

$$A_{i,drop} = 2\pi R^2(1 - \cos \theta) \quad (10)$$

$$A_{w,drop} = \pi R^2 \cos^2(\theta - \pi/2) \quad (11)$$

The projected area ( $A_{p,drop}$ ) is the footprint area of a droplet; the interfacial area ( $A_{i,drop}$ ) is the area of the liquid–vapor interface of a droplet; and the apparent wetted area ( $A_{w,drop}$ ) is the apparent area of the solid–liquid interface underneath a superhydrophobic droplet available to conduct heat to the substrate. Figure 7 shows the cumulative values of these areas, divided by the sample field of view area ( $A$ ).

The total surface heat flux shown in Figure 6c has been plotted in two distinct regions, an initial region of increasing nucleation site density and heat flux (lighter data) and a much larger region of decreasing nucleation site density and heat flux (darker data). The experimental uncertainty in the initial region is notably larger (>30%) than that calculated for the remainder of the data. This is due to the extremely small initial droplet sizes and the resulting uncertainty in droplet growth rate. Using

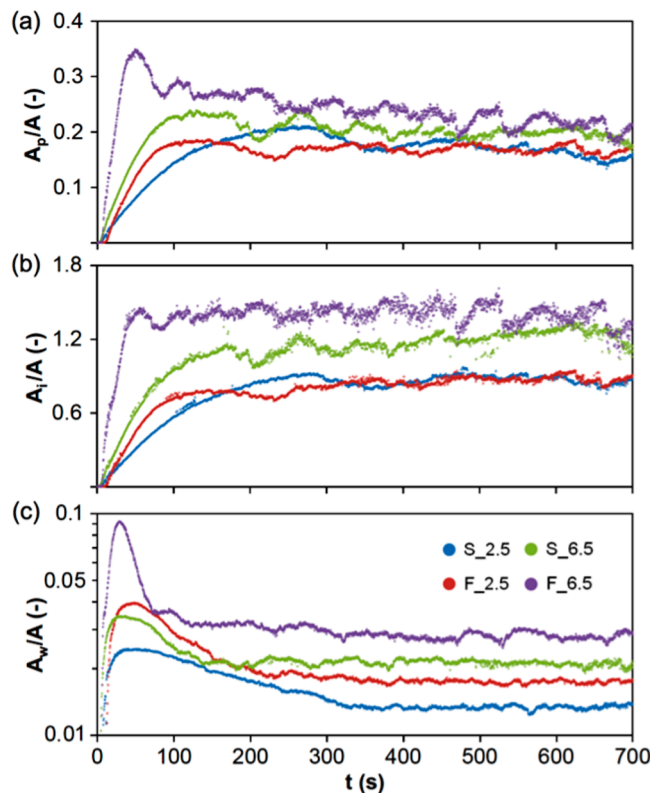


**Figure 7.** Dynamic (a) projected area ratio,  $A_p/A$ , (b) interfacial area ratio,  $A_i/A$ , and (c) apparent wetted area ratio,  $A_w/A$ , as a function of time for the four test conditions from Table 1. Experimental uncertainties are estimated to be  $\pm 5$ ,  $\pm 7$ , and  $\pm 5\%$ , respectively.

a 1 megapixel camera at 3 fps, heat flux has been measured with an accuracy of down to  $\pm 2 \text{ W/m}^2$ ; this is notably less than those reported using non-optical techniques relying on thermocouple measurements. While the characterization technique presented here has been used to measure relatively low heat fluxes (20–275  $\text{W/m}^2$  due to NCGs), its range and accuracy is dictated by the microscope optics, camera resolution, and frame rate alone. This measurement scheme can easily be extended to higher fluxes and measurement accuracies using larger optical magnification, camera resolution, and frame rate. While the frame rate used here (3 fps) was more than sufficient to accurately capture the droplet growth for the reported tests (hundreds of data points from nucleation to coalescence), the camera is capable of running at 2000 fps at full resolution and up to 300 000 fps at reduced resolution. This shows, that with the proper equipment and longer image processing times, this technique can be accurately applied to systems with heat fluxes several orders of magnitude higher than those measured here.

## RESULTS AND DISCUSSION

Figures 6 and 7 capture the dynamic behavior during superhydrophobic condensation under the loading conditions shown in Figure S4 and outlined in Table 1. These include time-varying droplet densities, active nucleation sites, wetting phenomena, and the resulting total surface heat flux. These parameters eventually reach steady state, showing the effects of saturation temperature difference and ramp rate on superhydrophobic condensation in the presence of NCGs. For each test, larger saturation temperature differences ( $\Delta T_{\text{sat}}^\infty$ ) lead to

higher nucleation site densities, smaller average droplet sizes, and higher heat fluxes, as would be expected. Additionally, it is seen that faster ramp rates lead to higher total surface heat fluxes due to increased nucleation site densities. This is due to the effects of NCGs in the very early stages of each test. Prior to applying the thermal ramping shown in Figure S4, there is essentially no heat flux across the surface. The concentration of water vapor near the interface is not affected by mass diffusion through the NCGs and, therefore, much higher than at steady state. By ramping quickly, the activation of more nucleation sites is possible by exposing the surface to both higher temperature differences as well as higher vapor concentrations in these very early stages. These effects are seen to have a critical impact on the steady-state performance of the surfaces. More nucleation sites lead to smaller coalescence lengths, resulting in surfaces with more droplets of smaller average size. Figure 7 shows three measures of the resulting wetting states and interfacial areas. As can be seen, for all cases the surface coverage (projected droplet area) was around 20% of the surface, but notable differences can be seen in the liquid–vapor and liquid–solid area ratios. Figure 7b shows that, depending on the loading conditions, the liquid–vapor interfacial area can be greater than ( $A_i/A > 1$ ) or less than ( $A_i/A < 1$ ) the actual area of the surface being tested, which is a potential means of heat transfer enhancement. Figure 7c shows that the apparent wetted area of the surface is only 1–3% of the actual surface area at steady state. Additionally, this steady-state apparent wetted area varied substantially with both thermal loading as well as ramp rate.

While Figures 6 and 7 show detailed information about the dynamic behavior of the relevant performance parameters during transient loading, it is more insightful to characterize the interdependence of these parameters. Figure 8 shows the

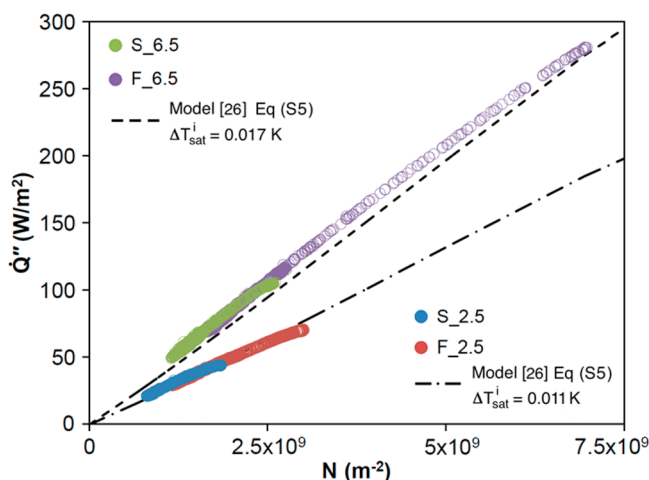


**Figure 8.** Experimentally measured total surface heat flux plotted relative to active nucleation site density for the four test conditions from Table 1, including predictions from analytical modeling.<sup>26</sup> The experimental uncertainties in  $\dot{Q}''$  and  $N$  are estimated to be  $\pm 17$  and  $\pm 4\%$ , respectively.

experimentally measured total surface heat flux relative to the nucleation site density for all four tests, plotted along with predictions from analytical modeling, showing excellent agreement. A nearly linear relationship can be seen for a given thermal loading, where over the course of a test the number of droplets on the surface varies (as seen in Figure 6a),

corresponding to variations in heat flux. This behavior is independent of ramp rate, showing higher heat fluxes at higher temperature differences as would be expected. This shows the importance of nucleation site density on enhancing heat transfer rates using jumping-mode superhydrophobic condensation. The model plotted in Figure 8 was developed by Miljkovic et al. for partially wetted droplets undergoing jumping-mode condensation on superhydrophobic nanostructured surfaces with dynamic contact angles.<sup>26</sup> This was created using predictions of heat transfer rates for individual droplets based on thermal circuit modeling, combined with predictions of droplet size distributions based on the work of Abu-Orabi<sup>61</sup> and Kim et al.<sup>62</sup> Details of the modeling approach can be found in the Supporting Information section 4.1.

The experimental measurements are based on growth rate and require empirically derived relationships (and their derivatives), which have been determined through dynamic measurements of droplets using the optical technique described above. The model, however, is based on thermal circuit analysis<sup>15,26</sup> using both material and geometric properties of the superhydrophobic surfaces, along with analytic predictions of droplet size distributions.<sup>15,26,61,62</sup> The consistency between these two approaches indicates that the technique developed to characterize dynamic heat flux is accurate well within the calculated uncertainty of  $\pm 17\%$ .

Figure 9 shows the heat transfer coefficient,  $h_c$ , as a function of both the coalescence length,  $L_c$ , as well as the apparent wetted area ratio,  $A_w/A$ , where the heat transfer coefficient is defined using the saturation temperature difference at the interface

$$h_c = \frac{\dot{Q}''}{\Delta T_{\text{sat}}^i} \quad (12)$$

The coalescence length is a measure of the average distance between nucleation sites (and droplet diameter at coalescence), and is defined as

$$L_c = \frac{1}{2\sqrt{N}} \quad (13)$$

assuming a Poisson distribution.<sup>13</sup> An inverse relationship between heat transfer coefficient and coalescence length can be seen, where smaller  $L_c$  leads to more densely packed nucleation sites and droplets, resulting in higher heat transfer. Additionally, excellent agreement is seen between the experimentally measured values and those predicted using analytical modeling (Supporting Information section 4.2). Figure 9b shows a definitive linear relationship between heat transfer coefficient and the apparent wetted area of the surfaces. Conversely, no discernible dependency was found by plotting heat transfer coefficient relative to the projected area ratio ( $A_p/A$ ) or the interfacial area ratio ( $A_i/A$ ). This suggests that heat conduction through the wetted base of the microscale droplets plays a critical role in the overall heat transfer rate. This is consistent with previously reported findings investigating single droplet growth rates using ESEM imaging.<sup>15</sup>

Due to the presence of NCGs, the maximum heat transfer coefficient measured here has been limited to  $h_c = 17 \text{ kW/m}^2$ . By defining  $h_c$  using the interfacial saturation temperature difference, the effects of mass diffusion through the NCGs and the associated reduction in saturation conditions near the droplets have been accounted for. However, the presence of NCGs still suppresses nucleation, thus reducing the active

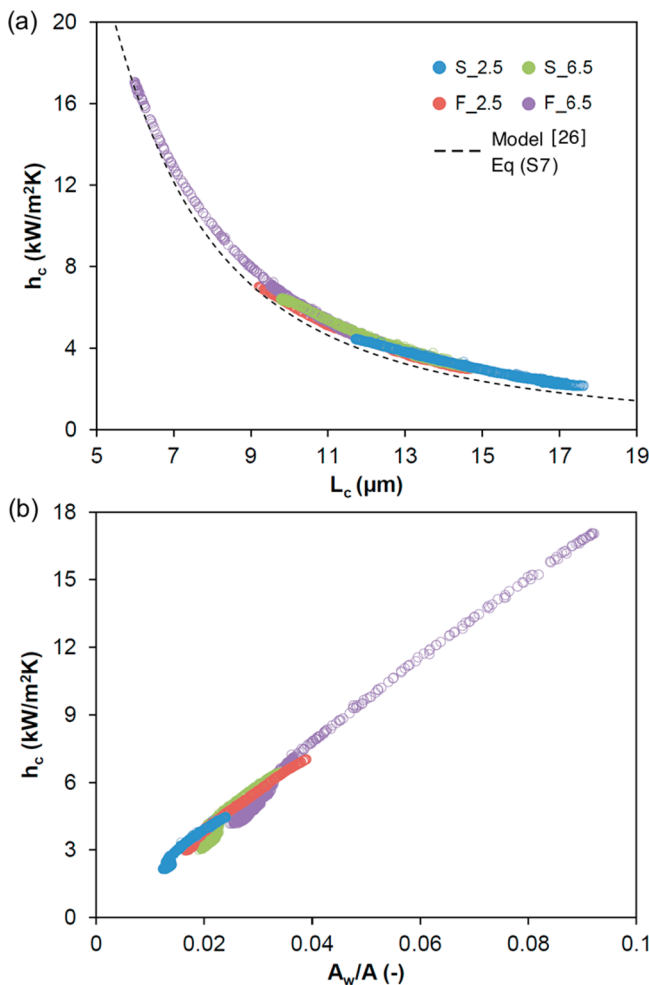


**Figure 9.** Experimentally measured heat transfer coefficient plotted relative to (a) coalescence length and (b) apparent wetted area ratio. Including (a) predictions from analytical modeling.<sup>26</sup> The experimental uncertainties in  $h_c$ ,  $L_c$ , and  $A_w/A$  are estimated to be  $\pm 18$ ,  $\pm 2$ , and  $\pm 5\%$ , respectively.

nucleation site density and increasing the coalescence length. The model shown in Figure 9a suggests that the surfaces would approach  $h_c \sim 90$  kW/m<sup>2</sup> (comparable to the results shown by Miljkovic et al. with no NCG<sup>1</sup>) at coalescence lengths of  $L_c \sim 2.5$  μm. Additionally, it has been shown that coalescence-induced ejection breaks down when the coalescence length approaches the characteristic nanostructure length scale.<sup>1,13,26</sup> The surfaces fabricated here, as seen in Figure 1 and Figure S1, have characteristic nanostructure heights of  $\sim 1$  μm, diameters of  $\sim 100$  nm, and spacings of  $\sim 500$  nm. This suggests that heat transfer coefficients approaching  $h_c \sim 1000$  kW/m<sup>2</sup> are theoretically possible before nanostructure flooding occurs. These predictions are speculative and the true performance would realistically depend on a variety of other factors. However, the approach presented in this work allows for the ability to dynamically measure relevant heat transfer and wetting parameters over a wide range of values, and ultimately characterize their interdependence. In contrast, other research in the field typically reports steady-state measurements (or no heat transfer measurements) at singular loading conditions and nucleation site densities.

## CONCLUSIONS

Sustained jumping-mode superhydrophobic condensation has been demonstrated using nanostructured coatings based on biotemplating of the *Tobacco mosaic virus*, combined with initiated chemical vapor deposition of thin PTFE films. The surfaces are robust, showing continued superhydrophobicity over several months with no degradation in performance after repeated testing. Using ESEM and optical microscopy, the droplet morphology, wetting dynamics, and condensation heat transfer performance of the virus-structured surfaces have been investigated in the presence of noncondensable gases. Full-field dynamic characterization of superhydrophobic condensation has been presented, for the first time, using a combination of optical microscopy and droplet image tracking. This allows for investigating the history of individual nucleation sites, droplets, and coalescence events, as well as measuring full-field dynamic behaviors of large sets of droplets. By quantifying the wetting morphology and growth rates of more than 3 million droplets over the course of four  $\sim 12$  min experiments, the surfaces have shown nucleation site densities of  $8 \times 10^8$  to  $7 \times 10^9$  m<sup>-2</sup>, coalescence lengths of 6–18 μm, and heat transfer coefficients of 2–17 kW/m<sup>2</sup>K. Using this technique, the importance of nucleation site density, coalescence length, and apparent wetted area ratio on overall heat transfer performance has been explicitly determined, leading to insights regarding the nature of superhydrophobic condensation as well as its enhancement through novel nanocoating designs.

## ASSOCIATED CONTENT

### Supporting Information

TMV biotemplating, initiated chemical vapor deposition, environmental scanning electron microscopy, experimental methods and apparatus, thermal circuit modeling, and uncertainty analysis. This material is available free of charge via the Internet at <http://pubs.acs.org>.

## AUTHOR INFORMATION

### Corresponding Author

\*E-mail: mccarthy@coe.drexel.edu.

### Notes

The authors declare no competing financial interest.

## ACKNOWLEDGMENTS

Support for this work was provided by the National Science Foundation (Grant No. CBET-1264958). The authors would like to acknowledge Prof. Ying Sun and the Complex Fluids and Multiphase Transport Lab, and Prof. Moses Noh and the Lab-on-a-Chip and BioMEMS Lab at Drexel University for the use of facilities critical to this work.

## REFERENCES

- (1) Miljkovic, N.; Enright, R.; Nam, Y.; Lopez, K.; Dou, N.; Sack, J.; Wang, E. N. Jumping-Droplet-Enhanced Condensation on Scalable Superhydrophobic Nanostructured Surfaces. *Nano Lett.* **2013**, *13* (1), 179–187.
- (2) Boreyko, J.; Chen, C.-H. Self-Propelled Dropwise Condensate on Superhydrophobic Surfaces. *Phys. Rev. Lett.* **2009**, *103* (18), 184501.
- (3) Chen, R.; Lu, M. C.; Srinivasan, V.; Wang, Z.; Cho, H. H.; Majumdar, A. Nanowires for Enhanced Boiling Heat Transfer. *Nano Lett.* **2009**, *9* (2), 548–553.
- (4) Choi, C.-H.; Kim, C.-J. C. Droplet Evaporation of Pure Water and Protein Solution on Nanostructured Superhydrophobic Surfaces of Varying Heights. *Langmuir* **2009**, *25* (13), 7561–7567.

- (5) Mishchenko, L.; Hatton, B.; Bahadur, V.; Taylor, J. A.; Krupenkin, T.; Aizenberg, J. Design of Ice-Free Nanostructured Surfaces Based on Repulsion of Impacting Water Droplets. *ACS Nano* **2010**, *4* (12), 7699–7707.
- (6) Rahman, M.; Ölçeroğlu, E.; McCarthy, M. Scalable Nano-manufacturing of Virus-Templated Coatings for Enhanced Boiling. *Adv. Mater. Interfaces* **2014**, *1* (2), 1300107.
- (7) Chen, C. H.; Cai, Q. J.; Tsai, C. L.; Chen, C. L.; Xiong, G. Y.; Yu, Y.; Ren, Z. F. Dropwise Condensation on Superhydrophobic Surfaces with Two-Tier Roughness. *Appl. Phys. Lett.* **2007**, *90* (17), 173108.
- (8) Chen, X. M.; Wu, J.; Ma, R. Y.; Hua, M.; Koratkar, N.; Yao, S. H.; Wang, Z. K. Nanograss Micropyramidal Architectures for Continuous Dropwise Condensation. *Adv. Funct. Mater.* **2011**, *21* (24), 4617–4623.
- (9) Feng, J.; Qin, Z.; Yao, S. Factors Affecting the Spontaneous Motion of Condensate Drops on Superhydrophobic Copper Surfaces. *Langmuir* **2012**, *28* (14), 6067–6075.
- (10) Lau, K.; Bico, J.; Teo, K.; Chhowalla, M.; Amarantunga, G.; Milne, W.; McKinley, G.; Gleason, K. Superhydrophobic Carbon Nanotube Forests. *Nano Lett.* **2003**, *3*, 1701–1705.
- (11) Koch, K.; Bhushan, B.; Jung, Y. C.; Barthlott, W. Fabrication of Artificial Lotus Leaves and Significance of Hierarchical Structure for Superhydrophobicity and Low Adhesion. *Soft Matter* **2009**, *5* (7), 1386–1393.
- (12) McCarthy, M.; Gerasopoulos, K.; Enright, R.; Culver, J. N.; Ghodssi, R.; Wang, E. N. Biotalemented Hierarchical Surfaces and the Role of Dual Length Scales on the Repellency of Impacting Droplets. *Appl. Phys. Lett.* **2012**, *100* (26), 263701.
- (13) Enright, R.; Miljkovic, N.; Al-Obeidi, A.; Thompson, C. V.; Wang, E. N. Condensation on Superhydrophobic Surfaces: The Role of Local Energy Barriers and Structure Length Scale. *Langmuir* **2012**, *28* (40), 14424–14432.
- (14) Guo, P.; Zheng, Y.; Wen, M.; Song, C.; Lin, Y.; Jiang, L. Icophobic/Anti-Icing Properties of Micro/Nanostructured Surfaces. *Adv. Mater.* **2012**, *24* (19), 2642–2648.
- (15) Miljkovic, N.; Enright, R.; Wang, E. N. Effect of Droplet Morphology on Growth Dynamics and Heat Transfer during Condensation on Superhydrophobic Nanostructured Surfaces. *ACS Nano* **2012**, *6* (2), 1776–1785.
- (16) Schimidt, E. S. W.; Sellschopp, W. Versuche über die Kondensation von Wasserdampf in Film- und Tropfenform. *Forsch. Ingenieurwes.* **1930**, *1*, 53–63.
- (17) Rose, J. W. Dropwise Condensation Theory and Experiment: A Review. *Proc. – Inst. Mech. Eng., Part A* **2002**, *216* (2), 115–128.
- (18) Dietz, C.; Rykaczewski, K.; Fedorov, A. G.; Joshi, Y. Visualization of Droplet Departure on a Superhydrophobic Surface and Implications to Heat Transfer Enhancement during Dropwise Condensation. *Appl. Phys. Lett.* **2010**, *97* (3), 033104.
- (19) Rykaczewski, K. Microdroplet Growth Mechanism during Water Condensation on Superhydrophobic Surfaces. *Langmuir* **2012**, *28* (20), 7720–7729.
- (20) Rykaczewski, K.; Paxson, A. T.; Anand, S.; Chen, X.; Wang, Z.; Varanasi, K. K. Multimode Multidrop Serial Coalescence Effects during Condensation on Hierarchical Superhydrophobic Surfaces. *Langmuir* **2013**, *29* (3), 881–891.
- (21) Rykaczewski, K.; Scott, J. H. J.; Fedorov, A. G. Electron Beam Heating Effects during Environmental Scanning Electron Microscopy Imaging of Water Condensation on Superhydrophobic Surfaces. *Appl. Phys. Lett.* **2011**, *98* (9), 093106.
- (22) Wang, F. C.; Yang, F. Q.; Zhao, Y. P. Size Effect on the Coalescence-Induced Self-Propelled Droplet. *Appl. Phys. Lett.* **2011**, *98* (5), 053112.
- (23) Peng, B. L.; Wang, S. F.; Lan, Z.; Xu, W.; Wen, R. F.; Ma, X. H. Analysis of Droplet Jumping Phenomenon with Lattice Boltzmann Simulation of Droplet Coalescence. *Appl. Phys. Lett.* **2013**, *102* (15), 151601.
- (24) Boreyko, J. B.; Zhao, Y.; Chen, C.-H. Planar Jumping-Drop Thermal Diodes. *Appl. Phys. Lett.* **2011**, *99* (23), 234105.
- (25) Boreyko, J. B.; Chen, C. H. Vapor Chambers with Jumping-Drop Liquid Return from Superhydrophobic Condensers. *Int. J. Heat Mass Transfer* **2013**, *61*, 409–418.
- (26) Miljkovic, N.; Enright, R.; Wang, E. N. Modeling and Optimization of Superhydrophobic Condensation. *J. Heat Transfer* **2013**, *135* (11), 111004.
- (27) Enright, R.; Miljkovic, N.; Dou, N.; Nam, Y.; Wang, E. N. Condensation on Superhydrophobic Copper Oxide Nanostructures. *J. Heat Transfer* **2013**, *135* (9), 091304.
- (28) Lee, S. Y.; Royston, E.; Culver, J. N.; Harris, M. T. Improved Metal Cluster Deposition on a Genetically Engineered Tobacco Mosaic Virus Template. *Nanotechnology* **2005**, *16* (7), S435–S441.
- (29) Gerasopoulos, K.; Pomerantseva, E.; McCarthy, M.; Brown, A.; Wang, C. S.; Culver, J.; Ghodssi, R. Hierarchical Three-Dimensional Microbattery Electrodes Combining Bottom-Up Self-Assembly and Top-Down Micromachining. *ACS Nano* **2012**, *6* (7), 6422–6432.
- (30) Gerasopoulos, K.; McCarthy, M.; Banerjee, P.; Fan, X.; Culver, J. N.; Ghodssi, R. Biofabrication Methods for the Patterned Assembly and Synthesis of Viral Nanotemplates. *Nanotechnology* **2010**, *21* (5), 055304.
- (31) Laird, E. D.; Bose, R. K.; Wang, W.; Lau, K. K. S.; Li, C. Y. Carbon Nanotube-Directed Polytetrafluoroethylene Crystal Growth via Initiated Chemical Vapor Deposition. *Macromol. Rapid Commun.* **2013**, *34* (3), 251–256.
- (32) Baxamusa, S. H.; Im, S. G.; Gleason, K. K. Initiated and Oxidative Chemical Vapor Deposition: A Scalable Method for Conformal and Functional Polymer Films on Real Substrates. *Phys. Chem. Chem. Phys.* **2009**, *11* (26), 5227–5240.
- (33) Pryce Lewis, H. G.; Bansal, N. P.; White, A. J.; Handy, E. S. HWCVD of Polymers: Commercialization and Scale-up. *Thin Solid Films* **2009**, *517* (12), 3551–3554.
- (34) Gerasopoulos, K.; Pomerantseva, E.; Fan, X.; Gnerlich, M.; Brown, A.; McCarthy, M.; Culver, J.; Ghodssi, R. Tobacco Mosaic Virus: An Integratable Biotalemented for Micro/Nano Systems. *J. Vac. Sci. Technol.* **2013**, *31*, 050815.
- (35) Fraenkel-Conrat, H.; Williams, R. C. Reconstitution of Active Tobacco Mosaic Virus from Its Inactive Protein and Nucleic Acid Components. *Proc. Natl. Acad. Sci. U.S.A.* **1955**, *41* (10), 690–698.
- (36) Balci, S.; Bittner, A. M.; Hahn, K.; Scheu, C.; Knez, M.; Kadri, A.; Wege, C.; Jeske, H.; Kern, K. Copper Nanowires within the Central Channel of Tobacco Mosaic Virus Particles. *Electrochim. Acta* **2006**, *51* (28), 6251–6257.
- (37) Sinan, B.; Kersten, H.; Peter, K.; Anan, K.; Christina, W.; Klaus, K.; Alexander, M. B. Electroless Synthesis of 3 nm Wide Alloy Nanowires Inside Tobacco Mosaic Virus. *Nanotechnology* **2012**, *23* (4), 045603.
- (38) Dujardin, E.; Peet, C.; Stubbs, G.; Culver, J. N.; Mann, S. Organization of Metallic Nanoparticles Using Tobacco Mosaic Virus Templates. *Nano Lett.* **2003**, *3* (3), 413–417.
- (39) Royston, E.; Ghosh, A.; Kofinas, P.; Harris, M. T.; Culver, J. N. Self-Assembly of Virus-Structured High Surface Area Nanomaterials and Their Application as Battery Electrodes. *Langmuir* **2007**, *24* (3), 906–912.
- (40) Gerasopoulos, K.; McCarthy, M.; Royston, E.; Culver, J. N.; Ghodssi, R. Nanostructured Nickel Electrodes Using the Tobacco Mosaic Virus for Microbattery Applications. *J. Micromech. Microeng.* **2008**, *18* (10), 104003.
- (41) Chen, X.; Gerasopoulos, K.; Guo, J.; Brown, A.; Ghodssi, R.; Culver, J. N.; Wang, C. High Rate Performance of Virus Enabled 3D n-Type Si Anodes for Lithium-Ion Batteries. *Electrochim. Acta* **2011**, *56* (14), 5210–5213.
- (42) Chen, X. L.; Gerasopoulos, K.; Guo, J. C.; Brown, A.; Wang, C. S.; Ghodssi, R.; Culver, J. N. A Patterned 3D Silicon Anode Fabricated by Electrodeposition on a Virus-Structured Current Collector. *Adv. Funct. Mater.* **2011**, *21* (2), 380–387.
- (43) Miller, R. A.; Presley, A. D.; Francis, M. B. Self-Assembling Light-Harvesting Systems from Synthetically Modified Tobacco Mosaic Virus Coat Proteins. *J. Am. Chem. Soc.* **2007**, *129* (11), 3104–3109.

- (44) Lau, K. K. S.; Mao, Y.; Pryce Lewis, H. G.; Murthy, S. K.; Olsen, B. D.; Loo, L. S.; Gleason, K. K. Polymeric Nanocoatings by Hot-Wire Chemical Vapor Deposition (HWCVD). *Thin Solid Films* **2006**, *501* (1–2), 211–215.
- (45) Martin, T. P.; Lau, K. K. S.; Chan, K.; Mao, Y.; Gupta, M.; Shannan O'Shaughnessy, W.; Gleason, K. K. Initiated Chemical Vapor Deposition (iCVD) of Polymeric Nanocoatings. *Surf. Coat. Technol.* **2007**, *201* (22–23), 9400–9405.
- (46) Yasuoka, H.; Yoshida, M.; Sugita, K.; Ohdaira, K.; Murata, H.; Matsumura, H. Fabrication of PTFE Thin Films by Dual Catalytic Chemical Vapor Deposition Method. *Thin Solid Films* **2008**, *516* (5), 687–690.
- (47) Henry, F.; Renaux, F.; Coppée, S.; Lazzaroni, R.; Vandencasteele, N.; Reniers, F.; Snyders, R. Synthesis of Superhydrophobic PTFE-like Thin Films by Self-Nanostructuration in a Hybrid Plasma Process. *Surf. Sci.* **2012**, *606* (23–24), 1825–1829.
- (48) Quade, A.; Polak, M.; Schröder, K.; Ohl, A.; Weltmann, K.-D. Formation of PTFE-like Films in CF4 Microwave Plasmas. *Thin Solid Films* **2010**, *518* (17), 4835–4839.
- (49) Tomi, S.; Béla, H.; Norbert, K. Pulsed Laser Deposition of Compact High Adhesion Polytetrafluoroethylene Thin Films. *J. Phys. D: Appl. Phys.* **2002**, *35* (15), 1859.
- (50) Burkarter, E.; Saul, C. K.; Thomazi, F.; Cruz, N. C.; Roman, L. S.; Schreiner, W. H. Superhydrophobic Electrosprayed PTFE. *Surf. Coat. Technol.* **2007**, *202* (1), 194–198.
- (51) Paxson, A. T.; Yague, J. L.; Gleason, K. K.; Varanasi, K. K. Stable Dropwise Condensation for Enhancing Heat Transfer via the Initiated Chemical Vapor Deposition (iCVD) of Grafted Polymer Films. *Adv. Mater.* **2014**, *26* (3), 418–423.
- (52) Bose, R. K.; Nejati, S.; Stufflet, D. R.; Lau, K. K. S. Graft Polymerization of Anti-fouling PEO Surfaces by Liquid-Free Initiated Chemical Vapor Deposition. *Macromolecules* **2012**, *45* (17), 6915–6922.
- (53) Lau, K. K. S.; Gleason, K. K. Initiated Chemical Vapor Deposition (iCVD) of Poly(alkyl acrylates): An Experimental Study. *Macromolecules* **2006**, *39* (10), 3688–3694.
- (54) Lau, K. K. S.; Gleason, K. K. Initiated Chemical Vapor Deposition (iCVD) of Poly(alkyl acrylates): A Kinetic Model. *Macromolecules* **2006**, *39* (10), 3695–3703.
- (55) Nejati, S.; Lau, K. K. S. Pore Filling of Nanostructured Electrodes in Dye Sensitized Solar Cells by Initiated Chemical Vapor Deposition. *Nano Lett.* **2011**, *11*, 419–423.
- (56) Bose, R. K.; Lau, K. K. S. Initiated CVD of Poly(2-hydroxyethyl methacrylate) Hydrogels: Synthesis, Characterization and In-Vitro Biocompatibility. *Chem. Vapor Depos.* **2009**, *15* (4–6), 150–155.
- (57) Torresin, D.; Tiwari, M. K.; Del Col, D.; Poulikakos, D. Flow Condensation on Copper-Based Nanotextured Superhydrophobic Surfaces. *Langmuir* **2013**, *29* (2), 840–848.
- (58) Beysens, D. The Formation of Dew. *Atmos Res.* **1995**, *39* (1–3), 215–237.
- (59) Fritter, D.; Knobler, C. M.; Beysens, D. A. Experiments and Simulation of the Growth of Droplets on a Surface (Breath Figures). *Phys. Rev. A* **1991**, *43* (6), 2858–2869.
- (60) Narhe, R. D.; Beysens, D. A. Water Condensation on a Super-Hydrophobic Spike Surface. *Europhys. Lett.* **2006**, *75* (1), 98–104.
- (61) Abu-Orabi, M. Modeling of Heat Transfer in Dropwise Condensation. *Int. J. Heat Mass Transfer* **1998**, *41* (1), 81–87.
- (62) Kim, S.; Kim, K. J. Dropwise Condensation Modeling Suitable for Superhydrophobic Surfaces. *J. Heat Transfer* **2011**, *133* (8), 081502.